The Astrophysical Journal, 999:170 (16pp), 2026 March 10 https://doi.org/10.3847/1538-4357/ae3c01

Modeling the Time-variable Broadband Emission and Correlation Study of FSRQ S5 1044+71

Sajad Ahanger[1], Shah Zahir[2], Sunder Sahayanathan[3,4], Naseer Iqbal[1], Malik Zahoor[5], and Aaqib Manzoor[6]
[1] Department of Physics, University of Kashmir, Srinagar, 19006, India; sajadphysics21@gmail.com
[2] Department of Physics, Central University of Kashmir, Ganderbal, 191201, India; shahzahir4@gmail.com
[3] Astrophysical Sciences Division, Bhabha Atomic Research Centre, Mumbai, 400085, India
[4] Homi Bhabha National Institute, Mumbai, 400094, India
[5] Department of Physics, National Institute of Technology, Srinagar 190006, India
[6] Indian Institute of Astrophysics, Bangalore 560034, India
Received 2025 November 16; revised 2026 January 5; accepted 2026 January 19; published 2026 March 2

Abstract

We present a detailed temporal and spectral analysis of the blazar S5 1044+71 using multiwavelength data obtained from the Fermi-LAT and Swift-XRT/UVOT telescopes. Applying the Bayesian block algorithm to the 3-day binned γ-ray light curve, we identify pronounced variability, including four major outbursts marked by significant flux enhancements. The highest flux recorded was $(1.1 \pm 0.2) \times 10^{-6}$ photons cm^{-2} s^{-1} on 57868.5 MJD. Each outburst comprises multiple components, and light-curve profile analysis indicates predominantly symmetric temporal structures. The shortest variability timescale of 4.5 hr constrains the emission region to be located within 0.03 pc of the central engine, likely near the broad-line region (BLR). Additionally, two highest-energy photons were detected with energies of 46.4 GeV (on 57739.6 MJD) and 42.5 GeV (on 59161.9 MJD), observed outside the peak flaring activity. The fractional variability shows an overall increasing trend from UV/optical to γ-ray bands, with a noticeable dip in the X-ray range, consistent with the shape of the broadband spectral energy distribution (SED). The flux distributions during flares exhibit lognormal or double-lognormal behavior, suggesting multiplicative variability processes and evolving emission zones. Cross-correlation analysis reveals a strong positive correlation between the γ-ray and X-ray bands, with X-rays lagging by 42.5 days. Broadband SED modeling across different flux states supports a one-zone leptonic scenario, with γ-ray emission produced via external Compton scattering of IR and BLR photons. High flux states show harder electron spectra, elevated break energies, and reduced magnetic fields—features consistent with efficient particle acceleration and Compton dominance.

Unified Astronomy Thesaurus concepts: Blazars (164); Active galaxies (17); Non-thermal radiation sources (1119); Relativistic jets (1390)

1. Introduction

Blazars, including BL Lac objects and flat-spectrum radio quasars (FSRQs), belong to a subclass of radio-loud active galactic nuclei (AGNs) with a relativistic jet pointing towards the Earth (C. M. Urry & P. Padovani 1995). BL Lac objects are characterized by weak optical emission lines or the absence of optical emission lines, in contrast to FSRQs, which exhibit such lines. The relativistic effects boost the intrinsic emission from blazars, making them some of the most luminous objects in the extragalactic Universe. The nonthermal emission from blazars has been detected across the entire electromagnetic spectrum with various ground- and space-based telescopes, spanning energy ranges from low-frequency radio to TeV-energy γ-rays. Moreover, blazars exhibit unique observational features such as large amplitude variability, high and variable polarization, compact radio emission, and high flux variability, with a variability timescale of the order of minutes to years (C. M. Urry & P. Padovani 1995; P. Padovani 2017; A. Goyal 2018).

The broadband spectral energy distribution (SED) of blazars feature a distinctive double-peaked structure. The low-energy peak, extending from optical and ultraviolet (UV) to X-ray energies, is attributed to Doppler-boosted synchrotron emission due to low-energy electrons in a magnetized jet (R. D. Blandford & M. J. Rees 1978; G. Ghisellini et al. 1989). The high-energy peak, which appears at γ-ray energies, can be interpreted through various models. The most widely accepted explanation involves the inverse Compton (IC) process, in which synchrotron photons, external photons, or both are upscattered to higher energies by relativistic particles within the jet. When synchrotron photons serve as the seed photons for IC scattering, the process is known as synchrotron self-Compton (SSC; G. Ghisellini et al. 1985; L. Maraschi et al. 1992; S. D. Bloom & A. P. Marscher 1996). If the seed photons originate outside the jet, such as from accretion disk, broad-line region (BLR), or dusty torus, the process is referred to as external Compton (EC; C. D. Dermer & R. Schlickeiser 1993; M. Sikora et al. 1994; Z. Shah et al. 2017; L. Costamante et al. 2018). Apart from leptonic models, another possible explanation for the high-energy component involves proton–synchrotron processes or proton cascades (K. Mannheim & P. L. Biermann 1992; W. Bednarek & R. J. Protheroe 1999; F. A. Aharonian 2000; A. Mücke & R. J. Protheroe 2001; S. Das et al. 2020). These processes are believed to be responsible for producing not only γ-ray photons but also high-energy neutrinos, therefore making leptohadronic models more favorable for explaining the broadband SED of blazars where neutrino detection is reported (N. Sahakyan 2018;

A. M. Bharathan et al. 2024; J. Robinson & M. Böttcher 2024). Based on the peak frequency ($\nu_{\rm syn}$) of the synchrotron component, blazars are further classified into three types: low-synchrotron-peaked (LSP; $\nu_{\rm syn} \leqslant 10^{14}$ Hz) blazars, intermediate-synchrotron-peaked (ISP; $10^{14} \leqslant \nu_{\rm syn} \leqslant 10^{15}$ Hz) blazars, and high-synchrotron-peaked (HSP; $\nu_{\rm syn} \geqslant 10^{15}$ Hz) blazars (A. A. Abdo et al. 2010a).

Blazar variability has been extensively studied to understand the nature of nonthermal emission and energy dissipation in relativistic jets. The variability timescales in blazars are generally classified into three categories: intraday (hours to days), short-term (days to months), and long-term (months to years). In the γ-ray band, flare timescales vary from minutes to hours, providing insights into the underlying physical properties, such as the location and size of the emission region, as well as jet dynamics (P. Kushwaha et al. 2014; V. S. Paliya 2015; M. Ackermann et al. 2016; N. Ding et al. 2019). However, the exact mechanisms responsible for these extreme γ-ray flares are still not fully understood. Apart from that, minute-scale variability poses significant challenges in explaining how broadband emission is produced near the supermassive black hole (SMBH) in such a compact region. Additionally, the underlying physical mechanism responsible for accelerating charged particles to relativistic speeds remains a complex issue. A variety of scenarios have been proposed to address these phenomena in blazars, including shock-in-jet models (M. Böttcher & C. D. Dermer 2010; MAGIC Collaboration et al. 2018), magnetic reconnection events (D. Giannios 2013; F. Guo et al. 2014; P. J. Morris et al. 2019), recollimation shock models (G. Bodo & F. Tavecchio 2018), and cloud-in-jet models (M. V. Barkov et al. 2012; A. T. Araudo et al. 2013; S. del Palacio et al. 2019). Furthermore, the flaring periods in blazars can vary depending on the underlying mechanism driving the flare. In the leptonic scenario, such flares are generally expected to produce correlated variability across multiple wave bands, often occurring nearly simultaneously. Under this scenario, relativistic electrons in the jet are responsible for both optical and γ-ray emissions, so a close correlation between their flux variations is expected (M. Böttcher 2007). Moreover, a correlation between different wave bands with negligible time lag has been found in many blazars (E. W. Bonning et al. 2009; R. Chatterjee et al. 2012; N. H. Liao et al. 2014; I. Liodakis et al. 2018). These results strongly support the one-zone leptonic model of blazar emission. Nevertheless, several studies challenge this model owing to the lack of correlation between flux variations among different wave bands. In such studies, there are instances where either γ-ray flares occur without their corresponding optical/X-ray flares (orphan γ-ray flares; M. S. Dutka et al. 2013; N. R. MacDonald et al. 2015; B. Rajput et al. 2020) or optical flares occur without their γ-ray/X-ray counterparts (orphan optical flares; R. Chatterjee et al. 2013; B. Rajput et al. 2019, 2020).

S5 1044+71 is a distant FSRQ at a redshift of $z \sim 1.15$ (A. G. Polatidis et al. 1995), associated with Fermi γ-ray source 4FGL J1048.4 +7143 (S. Abdollahi et al. 2020; J. Ballet et al. 2020). The source was classified as an LSP blazar in the second LAT AGN catalog (M. Ackermann et al. 2011), with R.A = 162.115083 and decl. = 71.726649. The Large Area Telescope (LAT) recorded γ-ray flaring activity from S5 1044+71 on 2013 March 1 and 2014 January 16–17 (R. Ojha et al. 2013; F. D'Ammando & M. Orienti 2014). Furthermore, on 2016 December 29, the γ-ray flux of the source increased significantly, reaching a maximum daily averaged flux ($E > 100$ MeV) of $(1.1 \pm 0.2) \times 10^{-6}$photons cm^{-2} s^{-1}, which is about 16 times higher than the average flux reported in the third Fermi-LAT catalog (3FGL; R. Ojha & B. Carpen 2017). The source exhibited near-infrared brightening in 2013 January, becoming approximately 1.2 mag brighter than its previous flux (L. Carrasco et al. 2013). On 2013 October 25, its R-band flux was observed in a flaring state about 1.5 mag brighter than its usual level (D. Blinov & A. Kougentakis 2013). Later, it entered a high-radio state between 2014 January and February (S. A. Trushkin et al. 2014a, 2014b). A significant optical enhancement was observed in 2017 January, with an R-band magnitude of 15.44 ± 0.20 (T. Pursimo et al. 2017), simultaneous with a γ-ray flare.

FSRQ S5 1044+71 has been investigated in several studies for possible quasi-periodic oscillations (QPOs). The analysis of a 5-day binned γ-ray light curve for the source revealed a potential QPO of 3.06 ± 0.43 yr, and the application of a binary black hole model suggests the existence of a binary SMBH at its center (G. G. Wang et al. 2022). A study of 24 bright AGNs by H. X. Ren et al. (2023) identified the longest QPO in S5 1044+71, with a period of approximately 1130 days. E. Kun et al. (2022) proposed a multimessenger model for the source, attributing flaring activity to the spin–orbit precession of a binary black hole based on Fermi-LAT γ-ray and very long baseline interferometry observations. They also expanded on the existing model and predicted the duration of the next γ-ray flare. A broadband spectral analysis of the high and low states of 12 distinct samples of Fermi-4LAC bright FSRQs, including S5 1044+71, using a log-parabola (LP) model was carried out to constrain the spectral parameters of the sources. The study revealed that the emission region in the jet exhibits a reduced radius during the high state, whereas the magnetic field strength increases during the low state (R. X. Zhou et al. 2024). Although many studies have been conducted, the underlying cause of blazar variability, as well as the location and origin of the γ-ray flares, is still not completely understood. In this work, we present a long-term multiwavelength study of the blazar S5 1044+71, utilizing observations from the Fermi-LAT, the Swift X-Ray Telescope (Swift-XRT), and Swift-UVOT. Specifically, we focus on the individual outburst phases recorded between 2008 August and 2024 March. While some outburst phases of S5 1044+71 have been previously studied, a comprehensive analysis covering all its outburst phases, short-timescale characteristics, and spectral evolution has not been presented in the literature. Our study also aims to investigate potential correlations between flux variations among different wave bands. Additionally, a detailed broadband SED modeling is carried out in different flux states of the source in order to constrain the underlying emission processes. The framework of this paper is as follows: In Section 2, we provide a brief description of the observations and data reduction methods. The results of the multiwavelength variability of S5 716+714 are presented in Section 3. The findings of the correlation study across different wave bands and the broadband spectral modeling are discussed in Sections 3.6 and 3.7, respectively. Finally, Section 4 provides the summary and discussion. Throughout this work, we used a flat Λ cold dark matter (ΛCDM) cosmology with $H_0 = 69.6$ km s^{-1} Mpc^{-1}, $\Omega_M = 0.29$, $\Omega_k = 0$, and $\Omega_\Lambda = 0.71$.

2. Observations and Data Analysis

In order to perform the multiwavelength analysis of the source S5 1044+71, we utilized publicly available data across the γ-ray, X-ray, ultraviolet (UV), and optical bands, covering a period of approximately 16 yr, from 2008 August to 2024 February.

2.1. Fermi-LAT Observations

Fermi-LAT is a pair-conversion γ-ray telescope sensitive to photon energies ranging from 20 MeV to >1 TeV. It surveys the entire sky approximately every 3 hr, with a field of view of $\sim$ 2.4 sr (W. B. Atwood et al. 2009). This setup is well suited for observing the short-term evolution of γ-ray point sources. Utilizing the Fermi-LAT public data server,[7] we collected the γ-ray data for S5 1044+71 from 2008 August 4 to 2024 February 5 (54682–60350 MJD), covering the energy range of 0.1–300 GeV.

We analyze the data using the LAT analysis software `FERMITOOLS` version 2.2.0, following the standard procedures outlined in the Fermi-LAT documentation.[8] The analysis is carried out using the `P8R3_SOURCE_V3` instrument response function. Photons are selected within a circular region of interest (ROI) with a 15° radius, centered at the location of S5 1044+71. Only photon-like events classified as `evclass` = 128 and `evtype` = 3 are selected. A zenith angle cut of <90° is applied to the data to reduce contamination from background γ-rays originating from the bright Earth's limb. The good time intervals, when the satellite was in standard data-taking mode, were selected using the filter expression `(DATA_QUAL > 0) && (LAT_CONFIG == 1)`. We modeled the Galactic diffuse emission and the isotropic emission components with `gll_iem_v07.fits` and `iso_P8R3_SOURCE_V3_v1.txt`, respectively. Utilizing the Fermi-LAT 4FGL catalog (S. Abdollahi et al. 2020), we generated an XML model file encompassing all sources within the ROI. During the analysis, the source parameters were left free within the ROI and constrained to their 4FGL catalog values outside ROI. To assess the significance of the detection, we used the maximum-likelihood test statistic (TS), defined as TS $=2\,\Delta\log(\mathcal{L})$, where $\mathcal{L}$ represents the likelihood function comparing models with and without a γ-ray point source at the source location. During the likelihood analysis, we froze the spectral parameters for the background sources with TS < 25 ($\sim 5\sigma$ detection), and the output model file is then used for the generation of light curves and spectra for the source. We considered source detection only when TS > 4, which corresponds to $\sim 2\sigma$ detection (J. R. Mattox et al. 1996).

2.2. Swift-XRT Observations

In this work, the X-ray data were collected by XRT on board the Neil Gehrels Swift Observatory (N. Gehrels et al. 2004), in the energy range of 0.3–10.0 keV. During the time period between 54682 and 60350 MJD, a total of 127 Swift observations were available for the source S5 1044+71. The Swift-XRT light curve is generated such that each observation ID corresponds to a single data point on the X-ray light curve. Moreover, for each γ-ray flare of the source, nearly simultaneous observations are also available in the X-ray light curve.

For the analysis, we followed the standard procedure provided by the instrumentation pipeline. We used only photon-counting (PC) mode data for the light curve and spectral analysis. The data were processed using the `xrtpipeline` version 0.13.7, incorporating the latest calibration database (CALDB; ver. 20190910) and response files from `HEASOFT` version 6.31.1. To generate the energy spectra, we added the calibrated and cleaned event files. The source spectra were extracted from a circular region with a radius of 20 pixels (1 pixel $\sim$ 2.″36), centered on the source, whereas the background spectra were extracted from a region with a radius of 50 pixels, located away from the source. The exposure maps were merged using the `ximage` task, while ancillary response files (ARFs) were generated using the task `xrtmkarf`. The corresponding response matrix files (RMFs) were retrieved from CALDB. Both the RMFs and ARFs were combined together with the source and background files using the tool `grppha`, such that each bin contains a minimum of 20 counts. Since the count rates for all the observations were significantly below 0.5 counts s^{-1}, pileup corrections were deemed unnecessary. The data were fitted with basic power-law (PL) and LP models, using `XSPEC`, version 12.13.0 (K. A. Arnaud 1996). During the fitting, the neutral hydrogen column density ($n_{\rm H}$) was set to $n_{\rm H} = 3.92 \times 10^{20}\,{\rm cm}^{-2}$ (P. M. W. Kalberla et al. 2005).

2.3. Swift-UVOT Observations

In addition to the X-ray data, Swift also provides optical/UV data through Swift-UVOT (P. W. A. Roming et al. 2005), which observes in optical and UV bands. The data obtained for S5 1044+71 were analyzed following the standard procedure using the `HEASOFT` package (ver. 6.31.1). The `UVOTSOURCE` task within the `HEASOFT` package was employed to process the images. The observations include all six filters: *v, b, u*, W1, M2, and W2. Multiple images from the various filters were combined using the `UVOTIMSUM` tool. We extracted the source counts from a circular region of 5″ radius centered on the source location, while the background counts were taken from a nearby source-free circular region with a radius of 10″. The observed fluxes were corrected for Galactic extinction using $E(B-V) = 0.0535$ and $R_V = A_V/E(B-V) = 3.1$, following E. F. Schlafly & D. P. Finkbeiner (2011).

3. Results

3.1. Long-term γ-Ray Temporal Analysis

The 3-day binned γ-ray light curve of S5 104+71 above 100 MeV, from 2008 August to 2024 February, is shown in Figure 1(a). All flux points displayed in the 3-day binned γ-ray light curve are obtained with TS > 4 (above 2σ detection). During the first 4 yr of LAT observations of S5 1044+71, the source remained largely in a steady state, with a mean flux of $(0.78 \pm 0.37) \times 10^{-7}$ photons $\rm cm^{-2}\,s^{-1}$. Following this period, the source exhibited four major γ-ray outburst phases (or flare epochs), showing significant flux variability, with flux reaching up to $(1.11 \pm 0.09) \times 10^{-6}$ photons $\rm cm^{-2}\,s^{-1}$ on 2017 April 25 (57868.5 MJD). In the 3-day binned γ-ray light curve, the flare epochs were identified by using the Bayesian block algorithm (J. D. Scargle et al. 2013). Here the Bayesian block algorithm was directly adopted from `astropy.stats` with a false-alarm rate parameter of $p_0 < 0.001$ (corresponding to $>3\sigma$). In order to determine the time range of the flare epochs, we apply Ivan Kramarenko's algorithm and

[7] https://fermi.gsfc.nasa.gov/cgi-bin/ssc/LAT/LATDataQuery.cgi
[8] https://fermi.gsfc.nasa.gov/ssc/data/analysis/documentation/

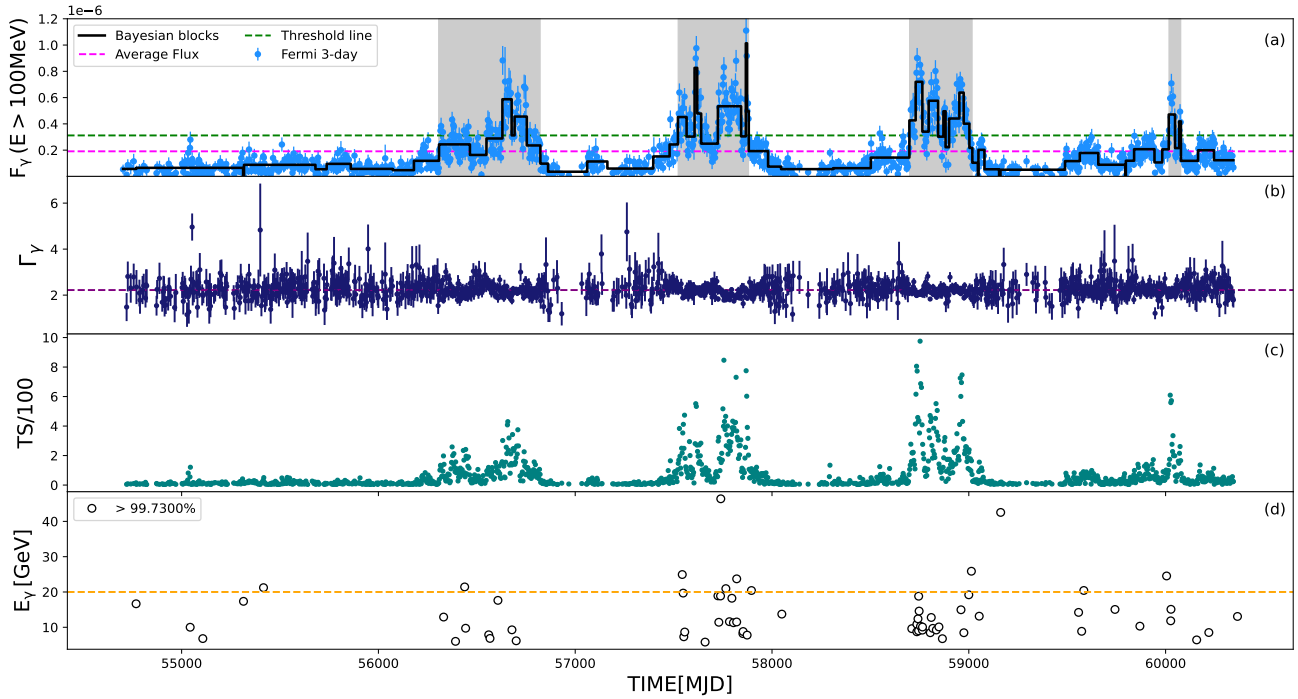

Figure 1. (a) Fermi-LAT light curve of S5 1044+71 from 2008 August to 2024 February at flux F_γ (E >100 MeV), with 3-day binning, in units of photons cm^{-2} s^{-1}. The gray vertical strips indicate the time intervals selected for the flux distribution study. (b) γ-ray spectral index (Γ_γ) as a function of time, with the horizontal dashed purple line representing the average value of the index. (c) TS values (>4) for each time bin. (d) Arrival times and energies of γ-ray photons E_γ, in units of GeV, with significance level above 3σ. All photons above the yellow dashed line have $E_\gamma > 20$ GeV.

consider monotonically decreasing sets of adjacent blocks. Following X. Geng et al. (2020) and A. K. Das et al. (2023), the algorithm uses an iterative approach to divide the light-curve data points into two sets: a low-state set and a high-state set or "anti-set." The threshold value for the flaring state is obtained as 3.12×10^{-7} photons cm^{-2} s^{-1} (dashed green line in Figure 1(a)). It is calculated by using the expression $\langle F\rangle + 2 \times F_{\rm Disp}$, where $\langle F\rangle$ is the mean flux of the light curve and $F_{\rm Disp}$ represents the true dispersion of the low-state group. Therefore, the determined flare epoch durations are represented as follows: 56306.5–56821.5 MJD for S1, 57523.5–57880.5 MJD for S2, 58699.5–59016.5 MJD for S3, and 60017.5–60076.5 MJD for S4; these are shown by shaded strips in Figure 1(a). In each epoch, the average flux exceeds the mean flux value of the entire γ-ray light curve, $(1.91 \pm 0.4) \times 10^{-7}$ photons cm^{-2} s^{-1} (Figure 1(a), dashed magenta line).

The γ-ray light curve of S5 1044+71 exhibits large flux variations, with each flare epoch consisting of multiple peaks. We study the temporal characteristics of the flare epochs and probe the evolution of the peak components during 55560.5–60344.5 MJD. We adopt the following sum of exponential (SOE) function to fit the temporal profile of the γ-ray light curve to compute the rise (T_r) and decay (T_d) times of each peak component (A. A. Abdo et al. 2010b):

$$F(t) = F_b + 2\sum_{i=1}^{n} F_{0,i} \times \left[\exp\left(\frac{t_{0,i} - t}{T_{r,i}}\right) + \exp\left(\frac{t - t_{0,i}}{T_{d,i}}\right)\right]^{-1}, \quad (1)$$

where i runs over the n major peaks, F_0 represents the photon flux at time t_0, and F_b denotes the baseline flux. For better photon statistics, we consider only flux points with a ratio of flux and error in flux $F/\delta F > 2$ and TS > 9 (significance $> 3\sigma$). The fitted SOE profile for the 3-day binned γ-ray light curves is shown in Figure 2. The time T_m of the maximum of a flare is given by (M. Hayashida et al. 2015)

$$T_m = T_0 + \frac{T_r T_d}{T_r + T_d} \ln\left(\frac{T_d}{T_r}\right), \quad (2)$$

where T_m is equal to T_0 when $T_r = T_d$. The symmetry of the flare components was obtained by

$$\xi = \frac{T_r - T_d}{T_r + T_d}, \quad (3)$$

where $|\xi| < 1$. For the components of the 3-day binned γ-ray light curve with peak flux exceeding 3.12×10^{-7} photons cm^{-2} s^{-1} (threshold line) and $\xi/\xi_{\rm err} \geqslant 2$, the best-fit parameters and their corresponding uncertainties are presented in Table 1. Further, flares with $\xi < 0$ are known as fast rise and exponential decay–type flares and are commonly observed in γ-ray light curves. These flares suggest that the injection of energetic particles occurs on timescales shorter than their subsequent cooling through radiative processes like IC scattering or synchrotron emission (M. Meyer et al. 2019; A. Thekkoth et al. 2024). However, in our analysis, we identified several flares with $\xi < 0$, with most flares displaying significant symmetry (Table 1).

To characterize the variability during different flaring epochs, we estimated the variability timescale of the source. We scanned the γ-ray light curve to determine the shortest flux doubling timescale by using the equation

$$F(t) = F(t_0)\, 2^{\frac{t-t_0}{\tau}}, \quad (4)$$

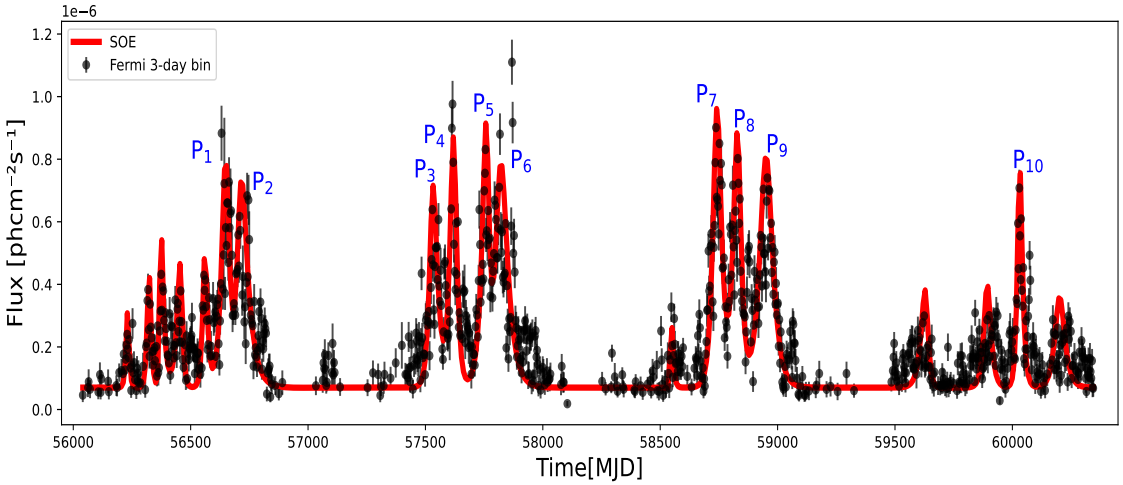

Figure 2. The 3-day binned γ-ray light curve of S5 1044+71 fitted with the SOE function defined in Equation (1).

Table 1
Rise and Decay Times for the 3-Day Bin γ-ray Light Curve Integrated over the Energy Range 0.1–300 GeV during 55560.5–60344.5 MJD

Peak	t_0 (MJD)	F_0 (10^{-7} photons cm^{-2} s^{-1})	T_r (days)	T_d (days)	ξ	$\xi/\xi_{\rm err}$
(1)	(2)	(3)	(4)	(5)	(6)	(7)
P_1	56650	7.24	15.37 ± 0.59	12.85 ± 1.10	0.08 ± 0.04	2.00
P_2	56710	6.09	12.48 ± 1.05	29.16 ± 0.86	−0.40 ± 0.03	13.34
P_3	57530	6.32	11.71 ± 0.56	17.69 ± 0.77	−0.20 ± 0.03	6.67
P_4	57620	7.91	13.30 ± 0.61	11.84 ± 0.44	0.05 ± 0.02	2.50
P_5	57762	7.57	17.93 ± 0.63	8.96 ± 0.74	0.33 ± 0.04	8.25
P_6	57817	7.01	17.49 ± 1.11	27.64 ± 0.72	−0.22 ± 0.03	7.33
P_7	58741	8.89	14.59 ± 0.44	16.73 ± 0.60	−0.06 ± 0.02	3.00
P_8	58830	7.99	16.03 ± 0.63	13.00 ± 0.48	0.10 ± 0.03	3.33
P_9	58950	7.40	22.95 ± 0.71	25.02 ± 0.59	−0.04 ± 0.02	2.00
P_{10}	60030	7.05	7.79 ± 0.38	10.55 ± 0.40	−0.15 ± 0.03	5.00

Note. Column (1): individual peaks. Columns (2) and (3): peak time (MJD) and peak flux (10^{-7} photons cm^{-2} s^{-1}). Columns (4) and (5): rise time and decay time of the components. Column (6): asymmetry parameter. Column (7): $\xi/\xi_{\rm err}$.

where $F(t)$ and $F(t_0)$ are the flux values measured at times t and t_0, with τ representing the characteristic flux doubling or halving time. On applying the condition that the significance of the difference in flux at time t and t_0 is $\geqslant 3\sigma$ (L. Foschini et al. 2011), we found the shortest variability timescale of 4.5 hr. The flux variability timescale can be used to constrain the size and location of the γ-ray emission region near the central black hole.

3.2. Search for Highest-energy Photon

We investigate the emission of high-energy γ-ray photons having energy $E_\gamma >$ 20 GeV. The observation of such photons is generally difficult to explain if the emission is assumed to originate only within the inner BLR, as photon–photon pair production would likely inhibit the escape of high-energy photons (A. C. Donea & R. J. Protheroe 2003; H. T. Liu et al. 2008; M. Böttcher et al. 2009). In order to search for high-energy photons associated with S5 1044+71, we utilized the `gtsrcprob` tool provided by the Fermi science package. This tool calculates the probability for the detected photons to be associated with the source ROI. Figure 1(d) shows the light curve of the high-energy photons, emitted over a period of around 15 yr, having $\geqslant$99.73% probability of originating from the source. The two highest-energy photons observed, with measured energies of 46.4 GeV at 57739.6 MJD and 42.5 GeV at 59161.9 MJD, each with a significance level of $>3\sigma$, are displayed in Figure 1(d). We note that both high-energy photons were detected outside the peak flaring activity of the source. Although the 46.4 GeV photon falls within the broader temporal interval associated with the second flaring epoch S2 (57523.5–57880.5 MJD), it is clearly offset from the flare maximum and coincides with a relatively low γ-ray flux state within that epoch. In general, enhanced γ-ray activity increases the probability of detecting high-energy photons; however, their detection during low flux states indicates that the conditions required for the production and escape of the highest-energy photons are not necessarily tied to peak flaring activity. The detection of ∼40–50 GeV photons from S5 1044 +71 can provide useful constraints on the physical conditions and location of the γ-ray emission region. The presence of such photons during low-activity phases suggests that they may originate from emission zones characterized by reduced soft-photon densities or enhanced Doppler boosting, which lowers the internal γ–γ opacity and facilitates photon escape (e.g., J. Poutanen & B. Stern 2010). In addition, attenuation by the extragalactic background light at these energies is expected to be moderate (J. D. Finke 2010), whereas absorption by local photon fields, particularly those associated with the BLR, can be significant if the emission region is located within the BLR.

Table 2
Spearman Rank Correlation Coefficient (r_s) and p-value for the Flaring Epochs S1–S4

Flare Epoch	r_s	p-value
S1	−0.03	6.63×10^{-1}
S2	−0.28	2.36×10^{-3}
S3	0.01	8.93×10^{-1}
S4	−0.13	5.94×10^{-1}

The detection of such high-energy photons therefore favors an origin at or beyond the BLR, or physical conditions that allow γ-rays to escape even during low flux states (e.g., F. Tavecchio et al. 2013).

3.3. γ-Ray Flux–Index Correlation

The flux versus index correlation is studied to find the association of index hardening or softening with different flux states. We used the Spearman rank correlation method to compute the correlation coefficient (r_s) and the null hypothesis probability (p) between the flux and index values for the selected epochs. The correlation analysis was performed with flux points having TS > 9 (significance $>3\sigma$) and signal-to-noise ratio $F/\delta F > 2$. The results of correlation analysis are provided in Table 2. We observed that epochs S1, S3, and S4 do not exhibit spectral hardening, while epoch S2 is characterized by a weak spectral hardening with $r_s = -0.28$ and $p = 2.36 \times 10^{-3}$. Moreover, a slight indication of mild negative correlation was observed during epoch S4, with a generally high scatter across all cases. A similar type of behavior has been noticed from several blazars, for example, PKS 1510–089 (A. A. Abdo et al. 2010a) and 3C 454.3 (M. Ackermann et al. 2010). The presence of a weak "harder-when-brighter" trend during the flare epoch S2 may indicate a temporary enhancement in particle acceleration efficiency or a hardening of the underlying electron energy distribution during this epoch. However, the correlation remains modest and is accompanied by substantial scatter, suggesting that statistical limitations and the possible overlap of multiple emission states likely affect the observed behavior. For the other epochs, the lack of a clear flux–index correlation may result from poorer photon statistics or the coexistence of multiple emission components. Therefore, while the observed behavior is qualitatively consistent with that reported for other blazars, the present data do not permit firm conclusions about the presence of distinct flaring or acceleration mechanisms across the different epochs.

3.4. Flux Distribution

The lognormal variability observed in blazar light curves is indeed an intriguing phenomenon. Many blazars exhibit typical lognormal flux distribution across different energy bands and timescales (H. E. S. S. Collaboration et al. 2010; Z. Shah et al. 2018). Analysis of Fermi-LAT light curves also indicates a predominant adherence of blazars to the lognormal flux distribution (M. Ackermann et al. 2015; Z. Shah et al. 2018; R. Prince et al. 2021). Such distributions can arise from multiplicative processes, such as the integration of numerous minijets, where the logarithm of the composite flux follows a normal distribution (J. Biteau & B. Giebels 2012). Moreover, introducing a Gaussian perturbation to the particle acceleration timescale can also lead to a lognormal flux distribution in blazar light curves (A. Sinha et al. 2018). In addition to single lognormal characteristics, flux histograms from certain blazars display a double lognormal distribution pattern (P. Kushwaha & M. Pal 2020). Furthermore, the presence of a double lognormal flux distribution in the X-ray emissions of blazars such as Mrk 501 and Mrk 421 has been attributed to the underlying dual Gaussian structure in the spectral index (R. Khatoon et al. 2020).

We analyzed the 3-day binned γ-ray light curve of S5 1044+71, during the flaring epochs S1, S2, S3, and S4, to study the flux distributions. To ensure good photon statistics, we include only flux points with $F/\delta F > 2$. To examine the flux characteristics of the source, we performed the Shapiro–Wilk (S-W) test (see, e.g., S. S. Shapiro & M. B. Wilk 1965; N. M. Razali et al. 2011), skewness, and histogram fitting test for all cases. The S-W test is a statistical tool that can be used to perform a normality test by evaluating the null hypothesis (H_0) that the data are drawn from a normal distribution. The test calculates the null hypothesis probability value (p-value), and if the p-value is $\leqslant 0.05$, the null hypothesis is rejected, suggesting that the sample deviates from the normal distribution. The S-W tests for flare epochs S1, S2, and S4 show that the p-values for 3-day binned fluxes in log-scale are greater than 0.05, indicating that the binned flux distributions are lognormal in nature (see Table 3). However, for S3 and the entire 3-day binned light curve, the p-values in both linear and log-scale are less than 0.05, suggesting that the binned flux distributions are neither normal nor lognormal. This result is further supported by the log-scale skewness test, where the TS values of –3.91 and 2.92, with p-values less than 0.05, indicate statistically significant skewness (see Table 3, last column).

We constructed histograms of normalized flux counts for the selected epochs and the entire 3-day binned light curve in log-scale. The histograms were generated such that each bin contains an equal number of flux points, while allowing the bin width to vary. The normalized flux histograms are plotted in Figure 3. We further analyzed the flux distributions by fitting their normalized histograms with a probability density function (pdf)

$$f(x) = \frac{1}{\sqrt{2\pi\sigma^2}} e^{-\frac{(x-\mu)^2}{2\sigma^2}}, \tag{5}$$

with μ and σ being the centroid and width of the distribution, respectively, and a double-pdf function (P. Kushwaha et al. 2016)

$$g(x) = \frac{a}{\sqrt{2\pi\sigma_1^2}} e^{-\frac{(x-\mu_1)^2}{2\sigma_1^2}} + \frac{(1-a)}{\sqrt{2\pi\sigma_2^2}} e^{-\frac{(x-\mu_2)^2}{2\sigma_2^2}}, \tag{6}$$

where a is a mixing fraction that determines the relative contribution of the two components and μ_1, μ_2 represent the centroids of the distributions with widths σ_1, σ_2, respectively. The corresponding lognormal or double lognormal fits to the histograms are shown in Figure 3, and the best-fit parameter values are provided in Table 4. The reduced χ^2 values suggest that the flux histograms from S1, S2, and S4 are lognormal, while the flux histograms from S3 and the entire 3-day binned γ-ray light curve are double lognormal in nature. Due to the small number of data points in S4, this result must be

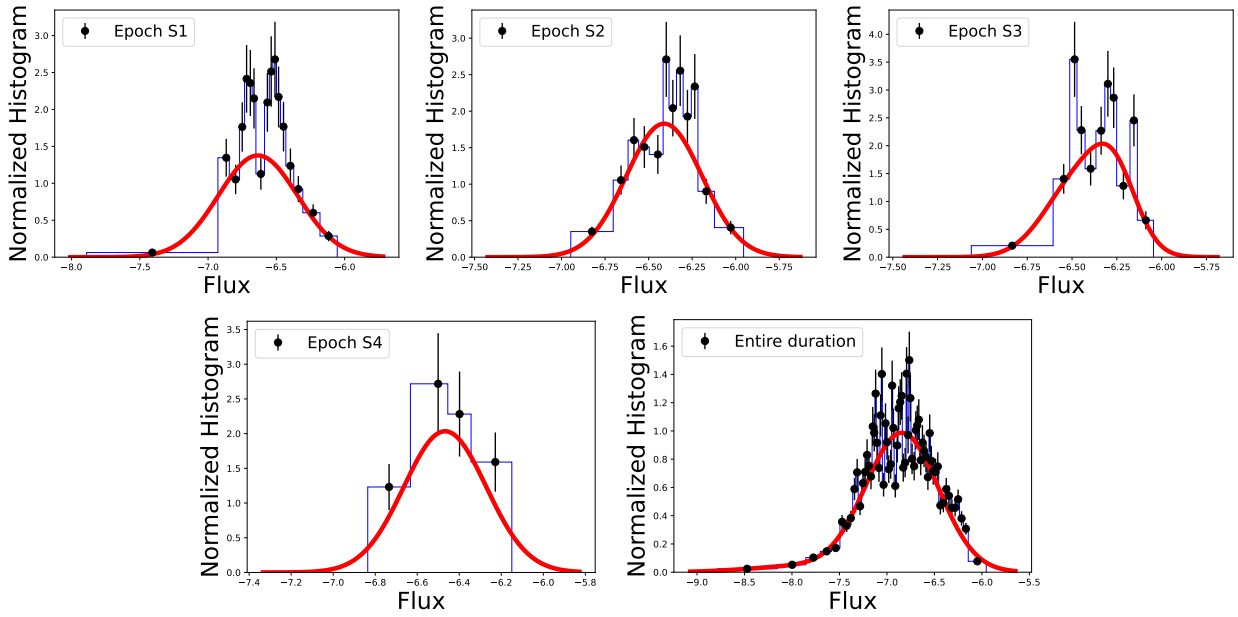

Figure 3. Flux distribution of S5 1044+71 in the γ-ray band. Epochs S1, S2, and S4 are fitted with a Gaussian pdf, whereas epoch S3 and the entire 3-day binned γ-ray light curve are fitted with a double Gaussian pdf. The fluxes are in units of photons cm^{-2} s^{-1}.

Table 3
Summary of S-W Test Results for Normal and Lognormal Distributions of Flux during Different Epochs

Epoch	Period	Number of Data Points	Normal Flux S-W (p-value)	Lognormal Flux	
				S-W (p-value)	Skewness (p-value)
S1	56306.5–56821.5	166	0.89 (1.53×10^{-9})	0.99 (0.34)	0.97 (0.33)
S2	57523.5–57880.5	117	0.94 (1.31×10^{-4})	0.98 (0.38)	−0.78 (0.43)
S3	58699.5–59016.5	106	0.98 (4.40×10^{-3})	0.94 (1.38×10^{-4})	−3.91 (8.9×10^{-5})
S4	60017.5–60076.5	21	0.95 (0.43)	0.94 (0.36)	−0.61 (0.53)
Entire duration	54702.5–60344.5	1320	0.85 (4.52×10^{-28})	0.98 (1.54×10^{-8})	2.92 (3.41×10^{-3})

Table 4
Best-fitting Parameter Values Obtained by Fitting Equations (5) and (6) to the Logarithm of the Fluxes in Different Selected Epochs

Epoch	Lognormal pdf		Double Lognormal pdf					χ^2_{red}
	μ	σ	a	μ_1	σ_1	μ_2	σ_2	
S1	−6.63 ± 0.03	0.28 ± 0.02	⋯	⋯	⋯	⋯	⋯	1.28
S2	−6.40 ± 0.02	0.21 ± 0.02	⋯	⋯	⋯	⋯	⋯	1.07
S3	⋯	⋯	0.34	−6.46 ± 0.12	0.18 ± 0.02	−6.26 ± 0.07	0.12 ± 0.03	1.68
S4	−6.44 ± 0.04	0.17 ± 0.05	⋯	⋯	⋯	⋯	⋯	0.91
Entire duration	⋯	⋯	0.06	−7.87 ± 0.09	0.54 ± 0.06	−6.83 ± 0.11	0.38 ± 0.03	1.12

interpreted as tentative. Furthermore, these results are also consistent with the results obtained from S-W test statistics.

3.5. Multiwavelength Light Curve

We generated the multiwavelength light curve of S5 1044+71 over a period of approximately 16 yr, from 2008 August 8 to 2024 February 4 (54702.5–60344.5 MJD). Figure 4 shows the multiwavelength light curve of the source constructed by combining the data obtained across γ-ray, X-ray, and optical/UV bands. Figure 4(a) shows the 7-day binned γ-ray light curve, obtained by integrating over the energy range 0.1–300 GeV, displaying multiple quiescent and flaring periods. Swift-XRT/UVOT made a total of 127 observations of the source with X-ray and optical/UV data analyzed by following the analysis procedure described in Section 2. Figures 4(b), (c), and (d) display the X-ray, UV, and optical light curves of the source, respectively. The multiplot illustrates the simultaneous flux variations across different energy bands. We observe that the γ-ray and optical/UV fluxes exhibit notable variations, whereas the X-ray flux shows only minimal fluctuations. We computed the variability of the source in each energy band by calculating the fractional rms variability amplitude (F_{var}) using the equation (S. Vaughan et al. 2003)

$$F_{var} = \sqrt{\frac{S^2 - \langle \sigma_{err}^2 \rangle}{\langle f \rangle^2}}, \quad (7)$$

where $\langle f \rangle$ is the mean flux, S^2 is the variance of the total number of flux points in the light curve, and $\langle \sigma_{err}^2 \rangle$ is their mean square

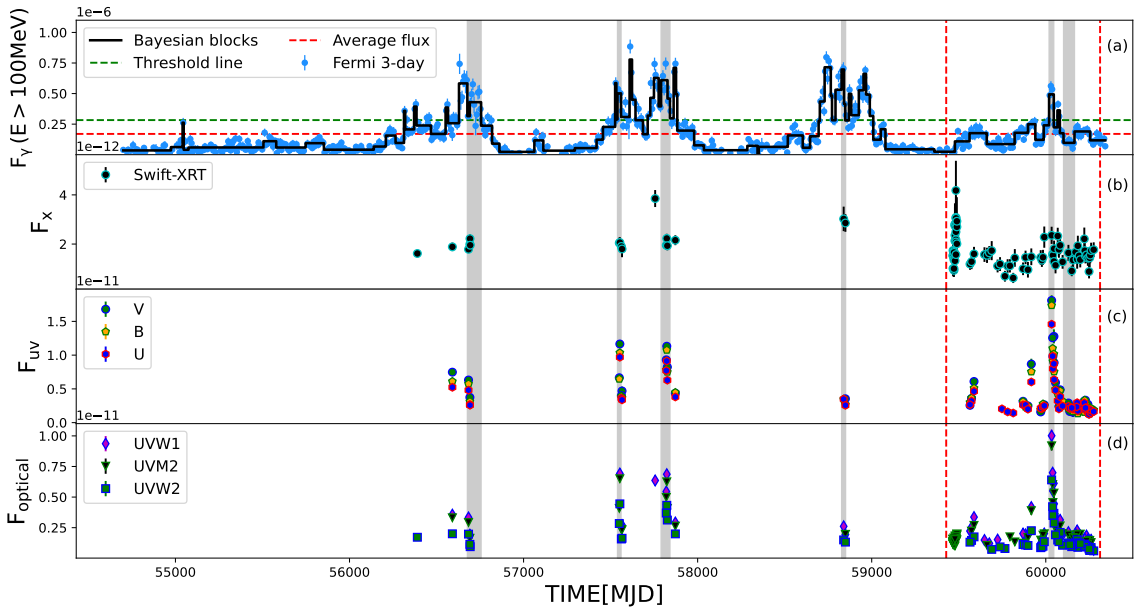

Figure 4. Multiwavelength light curves of S5 1044+71 obtained by using Fermi-LAT and Swift-XRT/UVOT observations. The observations spanned a period of 54702.5–60344.5 MJD. The top panel is the 7-day binned γ-ray light curve; the second, third, and fourth panels are the X-ray, UV, and optical band light curves, respectively. The gray vertical stripes indicate the regions where broadband spectral modeling is performed, while the region between the red vertical lines marks the time interval used for cross-correlation analysis among different bands.

Table 5
Fractional Variability Amplitude Obtained in γ-ray, X-Ray, Optical, and UV Energy Bands during 54702.5–60344.5 MJD

Energy Band	$F_{\rm var}$
γ-ray (0.1–300 GeV)	1.53 ± 0.001
X-ray (0.3–10 keV)	0.29 ± 0.022
UVOT band W2	0.67 ± 0.009
UVOT band M2	0.65 ± 0.008
UVOT band W1	0.68 ± 0.010
UVOT band *U*	0.73 ± 0.009
UVOT band *B*	0.74 ± 0.013
UVOT band *V*	0.76 ± 0.014

error. The uncertainty in $F_{\rm var}$ is given by (S. Vaughan et al. 2003)

$$(F_{\rm var})_{\rm err} = \sqrt{\frac{1}{2N}\left(\frac{\langle\sigma_{\rm err}^2\rangle}{F_{\rm var}\langle f\rangle^2}\right)^2 + \frac{1}{N}\frac{\langle\sigma_{\rm err}^2\rangle}{\langle f\rangle^2}}, \quad (8)$$

where N is the number of data points in the light curve. The obtained $F_{\rm var}$ values are presented in Table 5, and the plot of $F_{\rm var}$ versus energy is shown in Figure 5. The $F_{\rm var}$ shows an overall increasing trend from the UV/optical to the γ-ray band, with a noticeable dip in the X-ray range and a maximum observed in the γ-ray band. This trend in $F_{\rm var}$ can be potentially linked to the energy of relativistic electrons (M. Baloković et al. 2016; C. Chidiac et al. 2016) and is also evident from the broadband SED of blazars. The higher-energy electrons responsible for γ-ray emission, through the IC process, cool faster than low-energy electrons, resulting in faster variability in the γ-ray band.

3.6. Cross-correlation Analysis

The investigation of cross-correlation across different energy bands can reveal information about the radiation

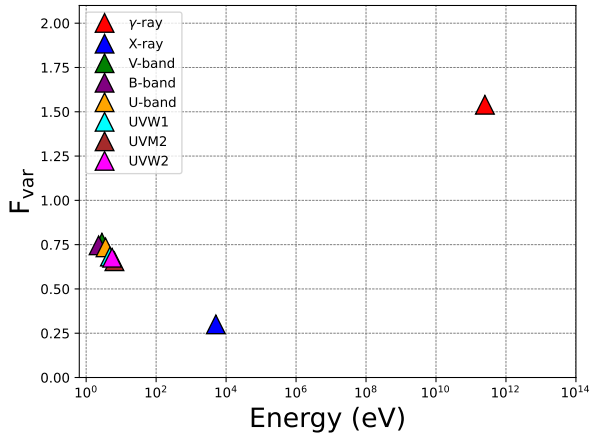

Figure 5. Fractional variability amplitude in the γ-ray, X-ray, optical, and UV bands plotted as a function of energy over the period 54702.5–60344.5 MJD.

mechanism and the location of the emission region in different bands (W. Max-Moerbeck et al. 2014a; V. Ramakrishnan et al. 2015; I. Liodakis et al. 2018). It can also be used to determine whether emissions in different bands are cospatial or arise from distinct regions within the jet (V. Ramakrishnan et al. 2016). We carried a cross-correlation analysis on γ-ray, X-ray, and UV–optical band light curves using the discrete correlation function (DCF). This method is ideal for handling discrete time-series data with uneven spacing, particularly for X-ray and UV–optical bands. The DCF calculates correlation coefficients directly without the use of interpolation across unevenly sampled data. The unbinned DCF (UDCF) for two datasets is defined by (R. A. Edelson & J. H. Krolik 1988)

$$\mathrm{UDCF}_{ij} = \frac{(a_i - \langle a\rangle)(b_j - \langle b\rangle)}{\sqrt{(\sigma_a^2 - e_a^2)(\sigma_b^2 - e_b^2)}}, \quad (9)$$

where a_i and b_i are the two discrete time series, and σ and e are the standard deviation and measurement error associated with each set, respectively. Here each value of UDCF_{ij} for the pair (a_i, b_j) is associated with the time delay $\Delta t_{ij} = t_j - t_i$. By averaging Equation (9) over M number of pairs for which $\tau - \Delta\tau/2 \leqslant \Delta t_{ij} (= t_j - t_i) \leqslant \tau + \Delta\tau/2$, we obtain the DCF given by

$$\mathrm{DCF}(\tau) = \frac{1}{M}\sum_{ij} \mathrm{UDCF}_{ij} \pm \sigma_{\mathrm{DCF}}(\tau), \tag{10}$$

where $\sigma_{\mathrm{DCF}}(\tau)$ is the associated error at time lag τ calculated as

$$\sigma_{\mathrm{DCF}}(\tau) = \frac{1}{M-1}\sqrt{\sum_{ij}[\mathrm{UDCF}_{ij} - \mathrm{DCF}(\tau)]^2}\,. \tag{11}$$

A positive correlation coefficient implies that the first time series leads the second, while a negative coefficient means that it lags the second.

The correlation study was carried for γ-ray with X-ray, optical (V, B, U), and UV (W1, M2, W2) wave bands. For robust correlation analysis, we chose a time period between 59428 and 60312 MJD, due to availability of closely spaced data points in all bands. The selected period is marked by red vertical lines in Figure 5, and the results of the correlation study are presented in Figure 6. We found that the γ-ray and X-ray flux points a show positive time lag of 42.5 days with a high DCF value of 0.94 ± 0.24. This suggests that light curves of γ-ray and X-ray bands show a strong positive correlation ($>3\sigma$), with X-ray lagging behind the γ-ray emission. Moreover, correlation of γ-ray with all optical and UV (W1, W2) bands shows a positive delay of 6.89 days with DCF values of 0.88 ± 0.18. Furthermore, it was found that the γ-ray and UV (M2) bands show no significant lag, with a DCF value of 0.84 ± 26, suggesting a cospatial emission region for these photons (see Figure 6). We also performed the Z-transformed DCF (zDCF) analysis (T. Alexander 2013) to verify whether the correlation coefficients were not due to DCF normalization. The zDCF yielded similar correlation coefficient values to the DCF results, with no new peaks detected.

The significance of the DCF is estimated by the Monte Carlo (MC) method introduced by W. Max-Moerbeck et al. (2014b). In the MC simulations, we generate 1000 random light curves for each band with a simple PL power spectral density (PSD; $P(\nu) \propto \nu^{\beta}$) following the algorithm described in J. Timmer & M. König (1995). The spectral index β for each band is determined by fitting the PSD of the actual observed light curve. Finally, the simulated light-curve pairs are cross-correlated to determine the significance level at each time lag. All the combinations demonstrated a strong correlation around the 99% level.

3.7. Spectral Energy Distribution and Its Modeling

In order to constrain the physical parameters responsible for simultaneous flux variations, we analyzed the broadband spectral properties of the source S5 1044+71. The analysis was conducted by selecting different time intervals from the multiwavelength light curve (see Figure 4). Due to the pronounced short-term variability of the source, we employed Bayesian analysis to divide the 7-day binned γ-ray light curve into smaller segments. Each segment of the γ-ray light curve is assumed to exhibit steady behavior in terms of the physical parameters. To select the Bayesian segments for broadband spectral analysis based on source activity and the availability of simultaneous γ-ray, X-ray, and UV/optical observations, we followed the approach mentioned in Section 3.1. Here the Bayesian block algorithm was adopted with a false-alarm probability $p_0 = 0.05$ ($\geqslant 95\%$). The selected time segments (or states), with peak γ-ray flux above the threshold line, are labeled as S1-A (56677–56756 MJD), S2-A (57539.5–57560 MJD), S2-B (57790–57841 MJD), S3-A (58827–58850 MJD), and S4-A (60019–60046 MJD). In addition to this, one quiescent flux state, characterized by a peak γ-ray flux below the threshold line, is identified and labeled as the state QS (60102–60165 MJD). The selected time segments are marked by gray vertical strips as shown in Figure 4. By comparing the results from different segments, one can identify the changes in the physical parameters responsible for the flux variations.

The γ-ray spectral curvature in blazars can reveal the intrinsic distribution of emitting electrons and provide valuable information about the possible acceleration and cooling mechanisms within the jets. We performed the γ-ray spectral analysis of the source S5 1044+71 by following the procedure outlined in Section 2.1. The γ-ray spectra in the considered flux states were fitted by using LP, PL, broken PL, and PL with an exponential cutoff (PLEC) models. The statistical significance of curvature/break in the γ-ray spectrum can be determined by using the equation (P. L. Nolan et al. 2012)

$$\mathrm{TS}_{\mathrm{curve}} = 2[\log \mathcal{L}(\mathrm{LP/BPL/PLEC}) - \log \mathcal{L}(\mathrm{PL})], \tag{12}$$

where $\mathcal{L}$ is the likelihood function. The curvature/break in the spectrum is considered significant only if $\mathrm{TS}_{\mathrm{curve}} > 16$, corresponding to the 4σ confidence level (J. R. Mattox et al. 1996). The results of this analysis, along with the obtained $\mathrm{TS}_{\mathrm{curve}}$ values, are summarized in Table 6, and the γ-ray spectra for the selected epochs are shown in Figure 7. The $\mathrm{TS}_{\mathrm{curve}}$ results indicate that γ-ray spectra of the states S1-A and S4-A exhibit a notable curvature, with the LP model providing the better fit statistics. However, the spectrum in these two states can be equally well described by the BPL/PLEC models in addition to the LP model. In the case of state S3-A, the PLEC model provides a statistically significant fit to the γ-ray spectrum (see Figure 7). Furthermore, the γ-ray spectra for S2-A, S2-B, and the quiescent state QS are well described by the PL model. The γ-ray SED plots, along with the corresponding model fits, are presented in Figure 7.

Based on the results of the γ-ray spectral analysis, we chose the γ-ray SED points from the best-fitted model of each state for the broadband SED modeling. The X-ray and UV–optical spectral points in each state were acquired by following the procedures mentioned in Section 2. However, the X-ray spectra are well fitted by the model tbabs*pow, except for state S3-A, where the spectrum is best described by tbabs*logpar. For the UVOT data, we note that its spectral shape deviates from the expected PL model. This suggests that the optical/UV flux may include additional emission components beyond the jet, likely associated with the accretion disk (S. Ahanger et al. 2025). Since the uncertainties in the optical/UV flux measurements are relatively small, the broadband spectral fitting can be influenced by this energy band. To mitigate this bias and allow for a more representative fit using a simple PL model, we added an additional systematic error of 5% to the optical/UV data. The broadband SED points

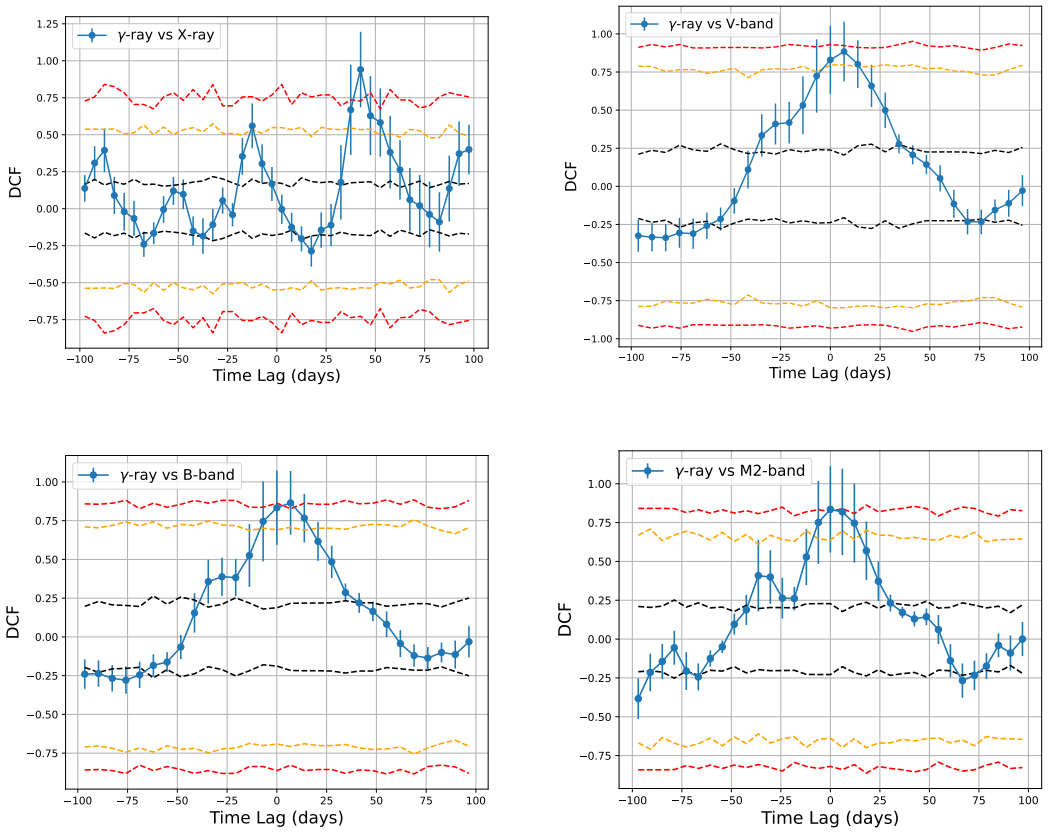

Figure 6. The outcomes of the discrete cross-correlation analysis conducted on the γ-ray with X-ray and optical (*V, B*) and UV (M2) band light curves during 59428–60312 MJD. The significance levels are represented by the black dashed line (68.27%, 1σ), orange dashed line (95.45%, 2σ), and red dashed line (99.73%, 3σ).

for states S1-A, S2-A, S2-B, S3-A, S4-A, and the quiescent state QS are shown in Figure 8.

The broadband SEDs of the source, in the selected flux states, are modeled using a one-zone leptonic model considering synchrotron, SSC, and EC processes (Z. Shah et al. 2017; S. Sahayanathan et al. 2018; S. Ahanger et al. 2025). This model considers the emission region as a spherical blob with radius R, moving along the blazar jet with a bulk Lorentz factor Γ and oriented at an angle θ to the observer. The emission region contains a nonthermal electron population characterized by a broken PL distribution

$$N(\gamma)\,d\gamma = \begin{cases} K\,\gamma^{-p}\,d\gamma & \text{for} \quad \gamma_{\rm min} < \gamma < \gamma_b \\ K\,\gamma_b^{q-p}\gamma^{-q}\,d\gamma & \text{for} \quad \gamma_b < \gamma < \gamma_{\rm max}, \end{cases} \tag{13}$$

where K is the normalization factor, γ represents the dimensionless energy of the electrons, $\gamma_{\rm min}$ and $\gamma_{\rm max}$ are the minimum and maximum dimensionless electron energies, respectively, p and q are the low- and high-energy spectral indices of the distribution, respectively, and γ_b is the break energy. These relativistic electrons, in the presence of a tangled magnetic field B, produce synchrotron emission. Additionally, they also undergo IC scattering, which includes the SSC and EC processes. For the EC emission, the target photons are assumed to be dominated by Lyα photons from the BLR and thermal IR photons from the molecular torus. The emissivity functions for the radiative processes (synchrotron, SSC, and EC) are computed numerically, and the resulting routines are incorporated as a local model in the XSPEC. For numerical simplicity, the BLR emission is approximated as a blackbody at a temperature of 42,000 K, equivalent to the Lyα line (2.47×10^{15} Hz), while the emission from the molecular torus is treated as a blackbody with a temperature of 1000 K. Under the synchrotron, SSC, and EC emission processes, the observed spectrum is primarily governed by 10 parameters. Among these, K, p, q, and γ_b describe the electron energy distribution; B, R, and θ characterize the macroscopic properties of the emission region; and two additional parameters represent the frequency and energy density of the external photon field. However, due to limited observational constraints in different energy bands, we adopted a minimalistic emission model. In this model, the spectral fit for different selected states was performed by setting all parameters free, except $\theta = 2°$, $R = 1.82 \times 10^{16}$ cm, $\gamma_{\rm max} = 2 \times 10^8$, and f (fraction of external scattered photons). The values of f for IR and BLR photons were fixed at $\sim 5.31 \times 10^{-2}$ and $\sim 10^{-7}$, respectively. Unlike other blazars where a single external photon field (from either the BLR or the IR torus) often provides a satisfactory fit to the γ-ray spectrum, our source required a contribution from both the BLR and the IR torus to reproduce the observed spectra in the selected flux states. The best-fit spectral model, which includes synchrotron, SSC, and EC (IR + BLR) components, along with the observed SED points for all selected states, is shown in Figure 8, and the corresponding fitting parameters are provided in Table 7.

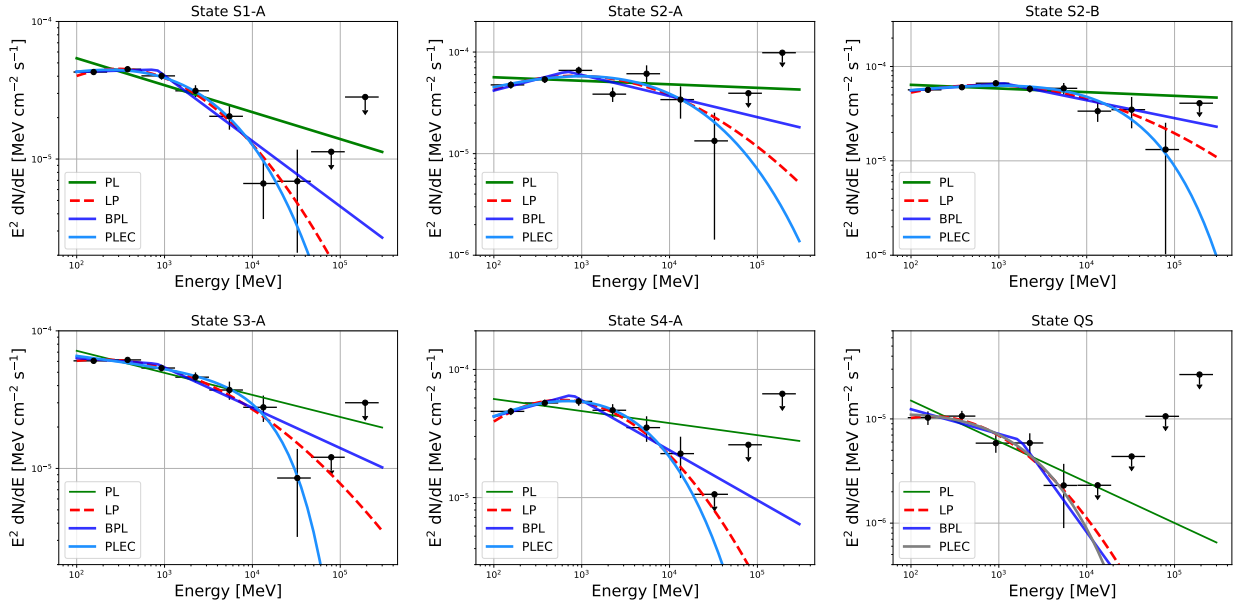

Figure 7. Plots of the γ-ray SEDs for different chosen epochs fitted with the spectral models shown. The details of the models are displayed within the insets in each plot.

Table 6
Results of γ-ray SED Analysis for Various Observed States

Flare Group/ States	$F_{0.1-300\ \mathrm{GeV}}$ (10^{-7} photons cm^{-2} s^{-1})	Power-law Γ			TS	$-\log(\mathcal{L})$	$\mathrm{TS}_{\mathrm{curve}}$
S1-A	4.5 ± 0.18	-2.19 ± 0.02	⋯	⋯	3112.13	−21768.03	⋯
S2-A	5.4 ± 0.36	-2.03 ± 0.02	⋯	⋯	1646.47	−9243.03	⋯
S2-B	6.1 ± 0.23	-2.03 ± 0.02	⋯	⋯	4410.15	−18591.85	⋯
S3-A	6.1 ± 0.22	-2.15 ± 0.02	⋯	⋯	4920.39	−22664.31	⋯
S4-A	5.3 ± 0.25	-2.71 ± 0.03	⋯	⋯	2307.28	−12554.29	⋯
QS	1.1 ± 0.12	-2.39 ± 0.07	⋯	⋯	286.88	−21244.86	⋯
⋯	⋯	Log-parabola	⋯	⋯	⋯	⋯	⋯
⋯	⋯	α	β	⋯	⋯	⋯	⋯
S1-A	4.1 ± 0.20	2.09 ± 0.03	0.10 ± 0.02	⋯	3139.13	−21754.99	26.08
S2-A	5.0 ± 0.39	1.97 ± 0.05	0.06 ± 0.02	⋯	1668.01	−9239.10	7.86
S2-B	5.8 ± 0.25	1.99 ± 0.02	0.04 ± 0.01	⋯	4424.54	−18586.24	11.22
S3-A	5.8 ± 0.21	2.10 ± 0.03	0.05 ± 0.01	⋯	4955.81	−22657.55	13.52
S4-A	4.8 ± 0.27	2.04 ± 0.04	0.12 ± 0.02	⋯	2357.31	−12541.28	26.02
QS	0.95 ± 0.14	2.38 ± 0.10	0.13 ± 0.07	⋯	289.89	−21242.71	4.30
⋯	⋯	Broken Power-law	⋯	$\epsilon_{\mathrm{break}}$	⋯	⋯	⋯
⋯	⋯	Γ_1	Γ_2	(GeV)	⋯	⋯	⋯
S1-A	4.1 ± 0.20	-1.98 ± 0.06	-2.41 ± 0.09	0.88 ± 0.23	3137.37	−21755.69	24.68
S2-A	4.9 ± 0.41	-1.77 ± 0.16	-2.20 ± 0.09	0.67 ± 0.39	1676.57	−9238.62	8.82
S2-B	5.8 ± 0.26	-1.92 ± 0.09	-2.13 ± 0.13	1.12 ± 0.41	4428.42	−18586.87	9.96
S3-A	5.9 ± 0.23	-2.04 ± 0.04	-2.29 ± 0.05	0.84 ± 0.09	4957.94	22659.47	9.68
S4-A	4.8 ± 0.27	-1.80 ± 0.08	-2.38 ± 0.10	0.78 ± 0.22	2353.42	−12542.58	23.42
QS	0.98 ± 0.24	-2.23 ± 0.40	-3.16 ± 4.51	1.74 ± 9.61	290.19	−21242.57	4.58
⋯	⋯	PLExpCutoff	⋯	$\epsilon_{\mathrm{cutoff}}$	⋯	⋯	⋯
⋯	⋯	Γ_{PLEC}	⋯	(GeV)	⋯	⋯	⋯
S1-A	4.2 ± 0.6	-1.71 ± 0.06	⋯	0.5 ± 0.10	3139.4	−21755.30	25.46
S2-A	5.08 ± 0.03	-1.73 ± 0.14	⋯	3.01 ± 0.54	1663.94	−9239.06	7.94
S2-B	5.8 ± 1.21	-1.89 ± 0.12	⋯	1.8 ± 0.25	4423.29	−18585.24	13.22
S3-A	5.9 ± 0.23	-2.08 ± 0.07	⋯	2.1 ± 0.97	4947.89	−22656.04	16.54
S4-A	4.9 ± 1.18	-1.53 ± 0.08	⋯	0.5 ± 0.17	2353.80	−12541.13	26.32
QS	0.96 ± 0.13	-1.80 ± 0.30	⋯	0.50 ± 0.95	290.30	−21242.59	0.24

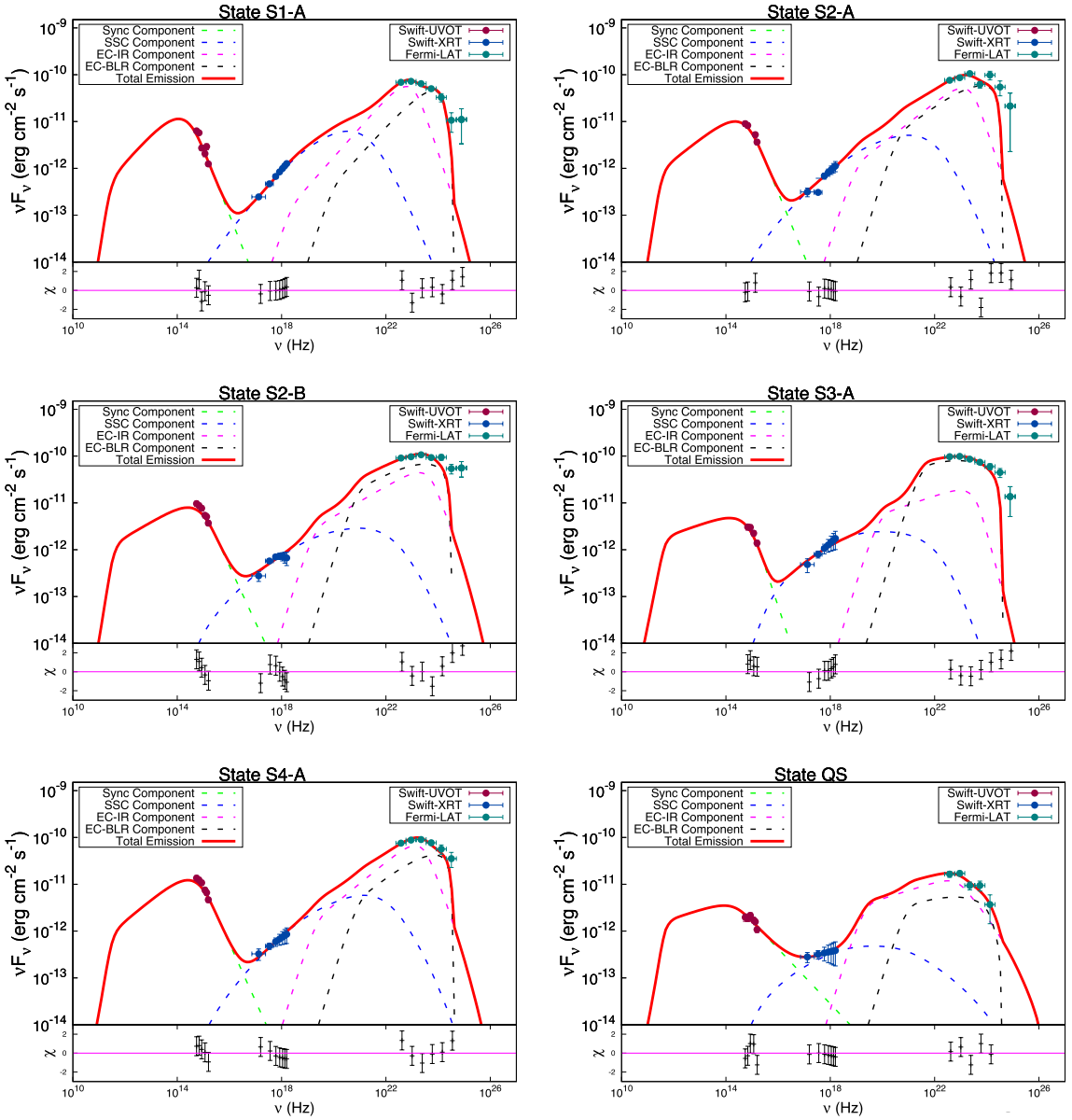

Figure 8. Broadband SEDs of S5 1044+71 obtained during different flux states. The solid red curve represents the combined best-fitting synchrotron, SSC, and EC spectrum.

Table 7
Optimal Parameters of the Broadband SED Modeling during Different Selected Periods

Parameter	Symbol	S1-A	S2-A	S2-B	S3-A	S4-A	QS
Low-energy particle index	p	$1.73^{+0.21}_{-0.19}$	$2.11^{+0.22}_{-0.21}$	$2.27^{+0.23}_{-0.22}$	$2.61^{+0.24}_{-0.20}$	$2.07^{+0.18}_{-0.17}$	$2.64^{+0.26}_{-0.28}$
High-energy particle index	q	$5.80^{+0.80}_{-0.71}$	$5.70^{+0.70}_{-0.68}$	$5.06^{--}_{-0.69}$	$6.36^{--}_{-0.70}$	$5.45^{+0.61}_{-0.61}$	$4.12^{+0.61}_{-0.66}$
Break Lorentz factor	γ_b	2092^{--}_{-408}	2871^{+466}_{-431}	3588^{+513}_{-461}	3377^{+496}_{-481}	3009^{+479}_{-445}	1622^{--}_{-321}
Minimum electron Lorentz factor	$\gamma_{\rm min}$	$11.31^{+2.23}_{-2.11}$	$18.48^{--}_{-3.12}$	$51.37^{--}_{-4.65}$	$50.01^{--}_{-4.31}$	$27.88^{+3.81}_{-3.62}$	$26.6^{+4.26}_{-4.03}$
Magnetic field (G)	B	$1.21^{--}_{-0.22}$	$1.24^{+0.18}_{-0.15}$	$0.96^{--}_{-0.23}$	$0.98^{+0.22}_{-0.17}$	$1.20^{+0.15}_{-0.11}$	$1.81^{+0.25}_{-0.19}$
Total jet power (log)	$P_{\rm jet}$	45.86	45.94	45.67	45.92	45.72	45.90
Equipartition	U_e/U_B	1.14	1.22	1.94	2.83	0.88	0.42
Reduced-χ^2 (χ^2/dof)	$\chi^2_{\rm red}$	13.25/12	14.88/12	21.13/13	16.50/11	9.62/11	7.36/10

4. Summary and Discussion

We analyzed 16 yr of Fermi-LAT observations to probe the high-energy emission characteristics of the source S5 1044 +71. The source displayed both long-term and short-term variability. During this period, the 3-day binned γ-ray light curve showed multiple outburst phases, with a peak flux of $(1.1 \pm 0.2) \times 10^{-6}$ photons cm^{-2} s^{-1} observed at 57751 MJD. This represents the highest 3-day binned γ-ray flux ever detected from the source. The 3-day binned γ-ray light curve is

also characterized by the temporal structure of the flare profiles. During our analysis, eight peaks exhibit symmetric profiles with $T_r \sim T_d(-0.3 \leqslant \zeta \leqslant 0.3)$, while two peaks show moderate asymmetry, with one peak showing $T_r < T_d(\zeta < -0.3)$ and the other showing $T_r > T_d(\zeta > 0.3)$ (see Table 1). Hence, most of the peaks have symmetric temporal profiles within the error bars. The detection of symmetric or asymmetric flares is closely related to the physical characteristics of the emitting region, such as spectral properties, the location of the peak flux with respect to energy, and the relevant acceleration and cooling timescales. In the case of a relativistic plasma propagating through a shock in the jet, the rise time corresponds to the duration over which the plasma enters the shock region, resulting in an increase in the number of accelerated electrons and, consequently, a rise in flux. The decay time reflects the period during which the plasma leaves the shock region, leading to a steady decrease in the number of energetic electrons and hence a decline in flux. Symmetric flares, where the rise and decay times are comparable, are expected when the radiative cooling time of the emitting particles is much shorter than the timescale of the shock–plasma interaction (R. D. Blandford & A. Königl 1979; R. Chatterjee et al. 2012). In this scenario, the observed symmetry in the temporal profiles suggests that both rise and decay phases are primarily governed by the plasma crossing time through the shock front. Conversely, asymmetric flares may occur when the interaction time is shorter than the characteristic acceleration or cooling timescales. Furthermore, Z. Shah et al. (2019) have shown that such asymmetry cannot be attributed merely to variations in the efficiency of the acceleration process, as such changes would produce similar behavior in both the rising and decaying phases. Instead, they demonstrated that asymmetry can arise as a result of a shift in the SED peak energy during the flare. For the source S5 1044 +71, the symmetric temporal profiles of the flares indicate that the rise and decay timescales are primarily governed by the crossing time of the radiation or a disturbance from a dense plasma blob moving through the shock front in the jet region. In a flare where the acceleration timescale is much shorter than the cooling timescale, the particles are energized more rapidly than they can lose energy through radiative processes such as synchrotron and IC cooling. Consequently, the acceleration region moves almost all the particles to their maximum energies. Once this acceleration phase is complete, the particles begin to cool slowly. As a result, the rise and decay times are not similar, leading to an asymmetric temporal profile (J. G. Kirk & A. Mastichiadis 1999). In this work, an asymmetric temporal profile would be expected to arise from the fast injection of accelerated particles or an escape from the emission region (see, e.g., M. Sikora et al. 2001; M. Joshi & M. Böttcher 2011; N. Roy et al. 2019).

The variability timescale of the source can be used to constrain the size of the emission region. An upper limit on the physical size of the γ-ray emission region can be calculated as

$$R \leqslant c\, t_{\rm var}\, \delta\, /(1+z). \tag{14}$$

Using the Doppler factor of $\delta = 20$ obtained through broadband SED modeling and a variability timescale of $t_{\rm var} = 4.5$ hr, we derive an upper limit on the size of the γ-ray emission region radius $R \sim 2.089 \times 10^{16}$ cm. This result is consistent with the results obtained by SED modeling but smaller than the value estimated by R. X. Zhou et al. (2024). The upper limit on the angular size (microarcseconds (μas)) of the emission region can be calculated using the formulation presented by B. Rani et al. (2013a, 2013b) as follows:

$$\phi \leqslant 173\, \frac{t_{\rm var}}{d_L}\, \delta\, (1+z)\ \mu{\rm as}, \tag{15}$$

where $t_{\rm var}$ is the variability timescale in years and $d_L = 7.9$ Gpc is the luminosity distance. We find that the angular size of the γ-ray emission region is $\sim$0.49 μas. The distance of the emission region along the jet axis can be constrained using the observed variability timescale, $d_\gamma \sim 2\, ct_{\rm var}\Gamma^2/(1+z)$. For blazars, the bulk Lorentz factor (Γ) of the radiating blob is typically $\Gamma \sim \delta$ (Doppler factor). Based on this, we calculate $d_\gamma \sim 0.0292$ pc (9.015×10^{16} cm), which places the emission region near the BLR ($R_{\rm BLR} \sim 3.4 \times 10^{17}$cm; R. X. Zhou et al. 2024). Hence, our result also indicates that a single-zone model, including EC emission from both the IR and the BLR components, should be able to accurately fit the broadband SEDs of the source.

The source displayed three major γ-ray outburst phases, each with a peak flux exceeding the threshold line (see Figure 1). The 3-day binned flux distribution of the flare epochs S1, S2, and S4 is consistent with a lognormal distribution. However, the binned flux distribution during the flare epoch S3 and the entire 3-day binned γ-ray light curve exhibit double lognormal behavior. This indicates that, unlike the other flare epochs, S3 may involve either multiple emission components or rapidly evolving physical conditions within the emission region. These features have also been reported in other bright blazars (see, e.g., P. Kushwaha et al. 2016; Z. Shah et al. 2018; F. Ait Benkhali et al. 2020; R. Khatoon et al. 2020). Hence, our results support the notion that the γ-ray emission regions or the dominant variability mechanisms can vary across different flare epochs, consistent with the conclusions of R. Prince et al. (2017). As demonstrated by A. Sinha et al. (2018), linear Gaussian fluctuations in the particle acceleration timescale naturally produce a single lognormal flux distribution, while variations in particle escape timescales can lead to non-Gaussian flux distribution. In this context, the single lognormal flux distributions observed in S1, S2, and S4 are consistent with a scenario dominated by Gaussian fluctuations in acceleration processes. In contrast, the double lognormal distribution observed in S3 implies either the coexistence of two emission components or a regime where variations in escape timescales become significant, leading to a double lognormal component in the flux distribution.

Over the past 16 yr, the source has demonstrated diverse flux variability, including periods of correlated GeV, X-ray, and optical/UV variations, as well as γ-ray flares without corresponding X-ray counterparts. We utilized the advanced DCF to investigate potential correlations between the γ-ray, X-ray, and optical/UV light curves. Our analysis revealed a strong positive correlation between the variations in optical/UV and γ-ray fluxes, particularly during the period 59428–60312 MJD, where γ-ray emission was found to lead the optical/UV emission by a few days. During the cross-correlation study of bright blazars, I. Liodakis et al. (2019) found that the time lag between the optical and γ-ray bands is generally small. Similarly, T. de Jaeger et al. (2023) reported that the time lag between these bands is generally consistent with zero. These findings suggest that the optical and γ-ray

flux emission regions are cospatial, supporting the leptonic emission model for blazars, with the same population of relativistic electrons responsible for both optical and γ-ray emissions. Since both fluxes are proportional to the number of emitting electrons, it is plausible that variations in the electron population within the jet drive the observed correlation between these flux variations, as suggested by F. D'Ammando et al. (2011). Furthermore, the γ-ray and X-ray flux variations exhibited a strong positive correlation ($>3\sigma$), with X-ray lagging behind the γ-ray emission by 42.5 days. Additionally, analysis using zDCF also revealed a positive correlation between the emissions across different bands. The DCF between the γ-ray and X-ray bands does not exhibit a single dominant peak but instead shows two peaks at different time lags (see Figure 6), indicating a complex correlation between the two bands. One possible explanation is the involvement of multiple external seed photon fields in the IC process responsible for the γ-ray emission, such as infrared photons from the dusty torus and photons from the BLR. In contrast, the X-ray emission is likely dominated by the SSC process, in which the same electron population produces synchrotron photons and subsequently upscatters them to X-ray energies. This difference in emission mechanisms can naturally lead to a more complex correlation structure between the γ-ray and X-ray bands. Consistent with this picture, the flux–flux correlation analysis indicates a strong correlation between the γ-ray and optical/UV bands, whereas the correlation between the γ-ray and X-ray bands appears more complex in nature. This complexity can be qualitatively connected to the lower fractional variability observed in the X-ray band (Section 3.5). Since the X-ray emission is likely dominated by low-energy electrons, its response to variations in the seed photon fields is expected to be weaker and slower than that of the γ-ray emission, which is governed by IC scattering involving higher-energy electrons. As a result, the different variability amplitudes and response timescales in the two bands may lead to multilag correlation rather than a single, well-defined correlation delay.

The temporal analysis of the multiwavelength light curves indicates that the source exhibits significant variability across all energy bands, with the lowest variability observed in the X-ray band and the highest variability in the γ-ray band (see Figure 5). The reduced variability in the X-ray band and the enhanced variability in the UV/optical and γ-ray bands can be naturally interpreted in the context of the energy distribution of relativistic electrons and the characteristic double-hump structure of blazar SEDs. The UV/optical and γ-ray bands are located near the peaks of the broadband SED, where the emission is dominated by high-energy electrons through synchrotron and IC processes (with both IR and BLR seed photons contributing in this work), respectively. In contrast, the X-ray emission at keV energies typically lies on the rising part or tail of the IC component and is mainly produced via SSC scattering by relatively low energy electrons. Consequently, the UV/optical and GeV emissions are governed by higher-energy electrons, while the X-ray emission is dominated by a lower-energy electron population, leading to a comparatively reduced variability amplitude in the X-ray regime. The observed highest variability amplitude in the γ-ray band relative to the X-ray and optical/UV bands is consistent with results from studies of other blazars (e.g., Y. H. Zhang et al. 2005; Z. Shah et al. 2019). This behavior can also be attributed to the more rapid radiative cooling of high-energy electrons compared to their low-energy counterparts, a scenario that is consistent with the symmetric flare profiles observed in the γ-ray band (see Section 3.1). Moreover, the increase in variability amplitude with photon energy may also reflect intrinsic spectral variability within the source (Y. H. Zhang et al. 2005).

To further investigate the underlying mechanism behind the γ-ray flares of S5 1044+71, we model the simultaneous multiband SEDs across the different flux states. The broadband SED in different flux states is well reproduced by a standard one-zone leptonic model including synchrotron, SSC, and EC components. In our fits, the high-energy γ-ray emission cannot be accounted for by either EC scattering of IR photons or EC scattering of BLR photons. Instead, both IR and BLR seed photon fields are required to reproduce the observed emission. In particular, we find that EC scattering of infrared photons extends up to the very high energy (VHE) end of the SED (avoiding Klein–Nishina suppression), while EC scattering of BLR photons suffers from KN suppression and accounts mostly for the GeV flux. This two-component EC scenario is invoked in other powerful FSRQs to match their double-humped SEDs (see, e.g., A. Barnacka et al. 2014). If we assume $\delta = 20$, the emission region can be located at $d_\gamma \simeq 0.0292$ pc from the nucleus. This is comparable to the canonical BLR radius ($\sim 3.4 \times 10^{17}$ cm; R. X. Zhou et al. 2024). This suggests that the emission region is likely located near the BLR, where both BLR and IR photon fields are sufficiently dense to contribute to the EC scattering process. We observe systematic trends in the model parameters from low to high flux states. In brighter states the particle energy distribution becomes flatter (indicating a harder spectrum), the electron break energy γ_b shifts to larger values, and the magnetic field strength B is reduced. Physically, a harder electron index and higher γ_b imply that the jet's acceleration processes are injecting a larger fraction of high-energy electrons during flares. At the same time, a weaker B-field reduces synchrotron cooling and makes the jet more particle dominated. This combination naturally pushes both SED peaks to higher frequencies and increases the Compton dominance. Qualitatively, our result—a "harder-when-brighter" electron spectrum coupled with lower B in the high flux states—is consistent with similar findings in other blazars. For example, multiepoch SED modeling of 3C 279 showed that the high state exhibited a slightly reduced magnetic field and a flatter electron spectrum compared to the quiescent state (Z. Shah et al. 2019; A. Tolamatti et al. 2022; G. Wang et al. 2022). Such behavior has also been seen in PKS 1510–089 and CTA 102 flares, where flaring states required an injection of very energetic electrons (high γ_b) and sometimes a lower B. In contrast, some other studies (e.g., J. Majumdar et al. 2025 on FSRQ 4C+27.50) report increases in B and Doppler factor during flares, underscoring that multiple mechanisms may drive different outbursts. In our case, the consistently higher γ_b and harder spectra at high flux imply more efficient acceleration when the jet is most active. Since we infer that the emission region lies near the BLR, the reduced B could also indicate that the flaring zone moves slightly beyond the inner BLR, where field strength drops; in that case IC scattering of IR photons could further dominate. The dominance of IC scattering of IR photons is further supported by the detection of $\sim$40–50 GeV photons (see Section 3.2),

which escape without significant γ–γ absorption, also suggesting that the emission region is not located deep within the BLR but is instead situated at or beyond the BLR. Overall, the parameter evolution—harder electron spectrum, weaker B, and higher break energy in the high state—is qualitatively consistent with a picture where during outbursts a larger fraction of jet power is channeled into relativistic electrons. Future observations of the source, particularly in the VHE γ-ray regime, will be crucial for rigorously testing these scenarios, as they will probably better constrain the location of the emission region and the dominant radiative processes during different activity states.

Acknowledgments

The authors thank the anonymous referee for valuable comments and suggestions. The authors thank the Department of Physics, University of Kashmir for providing the necessary facilities to carry out this research. S.Z. is supported by the Department of Science and Technology (DST), Government of India, under the INSPIRE Faculty grant (DST/INSPIRE/04/2020/002319). M.Z. acknowledges the financial support provided by the Science and Engineering Research Board (SERB), Government of India, under the National Postdoctoral Fellowship (NPDF), Fellowship reference no. PDF/2023/002995. S.A. also thanks IUCAA for providing the facilities. This research has made use of γ-ray data from the Fermi Science Support Center (FSSC). The work has also used the Swift data from the High Energy Astrophysics Science Archive Research Center (HEASARC), at NASA's Goddard Space Flight Center.

Data Availability

The data and the model used in this article will be shared on reasonable request to the corresponding author, Sajad Ahanger (email: sajadphysics21@gmail.com).

ORCID iDs

Shah Zahir https://orcid.org/0000-0003-1458-4396
Malik Zahoor https://orcid.org/0000-0002-8955-3212

References

Abdo, A. A., Ackermann, M., Agudo, I., et al. 2010a, ApJ, 716, 30
Abdo, A. A., Ackermann, M., Ajello, M., et al. 2010b, ApJ, 722, 520
Abdollahi, S., Acero, F., Ackermann, M., et al. 2020, ApJS, 247, 33
Ackermann, M., Ajello, M., Allafort, A., et al. 2011, ApJ, 743, 171
Ackermann, M., Ajello, M., Atwood, W. B., et al. 2015, ApJ, 810, 14
Ackermann, M., Ajello, M., Baldini, L., et al. 2010, ApJ, 721, 1383
Ackermann, M., Anantua, R., Asano, K., et al. 2016, ApJL, 824, L20
Ahanger, S., Sahayanathan, S., Jagan, S. K., Zahir, S., & Iqbal, N. 2025, JHEAp, 47, 100400
Aharonian, F. A. 2000, NewA, 5, 377
Ait Benkhali, F., Hofmann, W., Rieger, F. M., & Chakraborty, N. 2020, A&A, 634, A120
Alexander, T. 2013, arXiv:1302.1508
Araudo, A. T., Bosch-Ramon, V., & Romero, G. E. 2013, MNRAS, 436, 3626
Arnaud, K. A. 1996, ASPC, 101, 17
Atwood, W. B., Abdo, A. A., Ackermann, M., et al. 2009, ApJ, 697, 1071
Ballet, J., Burnett, T. H., Digel, S. W., & Lott, B. 2020, arXiv:2005.11208
Baloković, M., Paneque, D., Madejski, G., et al. 2016, ApJ, 819, 156
Barkov, M. V., Aharonian, F. A., Bogovalov, S. V., Kelner, S. R., & Khangulyan, D. 2012, ApJ, 749, 119
Barnacka, A., Böttcher, M., & Sushch, I. 2014, ApJ, 790, 147
Bednarek, W., & Protheroe, R. J. 1999, MNRAS, 302, 373
Bharathan, A. M., Stalin, C. S., Sahayanathan, S., Bhattacharyya, S., & Mathew, B. 2024, MNRAS, 529, 3503
Biteau, J., & Giebels, B. 2012, A&A, 548, A123
Blandford, R. D., & Königl, A. 1979, ApJ, 232, 34
Blandford, R. D., & Rees, M. J. 1978, in Pittsburgh Conf. on BL Lac Objects, ed. A. M. Wolfe (Univ. Pittsburgh), 328
Blinov, D., & Kougentakis, A. 2013, ATel, 5512, 1
Bloom, S. D., & Marscher, A. P. 1996, ApJ, 461, 657
Bodo, G., & Tavecchio, F. 2018, A&A, 609, A122
Bonning, E. W., Bailyn, C., Urry, C. M., et al. 2009, ApJL, 697, L81
Böttcher, M. 2007, Ap&SS, 309, 95
Böttcher, M., & Dermer, C. D. 2010, ApJ, 711, 445
Böttcher, M., Reimer, A., & Marscher, A. P. 2009, ApJ, 703, 1168
Carrasco, L., Recillas, E., Porras, A., Mayya, D. Y., & Carraminana, A. 2013, ATel, 4815, 1
Chatterjee, R., Bailyn, C. D., Bonning, E. W., et al. 2012, ApJ, 749, 191
Chatterjee, R., Fossati, G., Urry, C. M., et al. 2013, ApJL, 763, L11
Chidiac, C., Rani, B., Krichbaum, T. P., et al. 2016, A&A, 590, A61
Costamante, L., Cutini, S., Tosti, G., Antolini, E., & Tramacere, A. 2018, MNRAS, 477, 4749
D'Ammando, F., & Orienti, M. 2014, ATel, 5784, 1
D'Ammando, F., Raiteri, C. M., Villata, M., et al. 2011, A&A, 529, A145
Das, A. K., Mondal, S. K., & Prince, R. 2023, MNRAS, 521, 3451
Das, S., Gupta, N., & Razzaque, S. 2020, ApJ, 889, 149
de Jaeger, T., Shappee, B. J., Kochanek, C. S., et al. 2023, MNRAS, 519, 6349
del Palacio, S., Bosch-Ramon, V., & Romero, G. E. 2019, A&A, 623, A101
Dermer, C. D., & Schlickeiser, R. 1993, ApJ, 416, 458
Ding, N., Gu, Q. S., Geng, X. F., et al. 2019, ApJ, 881, 125
Donea, A. C., & Protheroe, R. J. 2003, PThPS, 151, 186
Dutka, M. S., Ojha, R., Pottschmidt, K., et al. 2013, ApJ, 779, 174
Edelson, R. A., & Krolik, J. H. 1988, ApJ, 333, 646
Finke, J. D. 2010, arXiv:1005.2626
Foschini, L., Ghisellini, G., Tavecchio, F., Bonnoli, G., & Stamerra, A. 2011, A&A, 530, A77
Gehrels, N., Chincarini, G., Giommi, P., et al. 2004, ApJ, 611, 1005
Geng, X., Zeng, W., Rani, B., et al. 2020, ApJ, 904, 67
Ghisellini, G., George, I. M., & Done, C. 1989, MNRAS, 241, 43P
Ghisellini, G., Maraschi, L., & Treves, A. 1985, A&A, 146, 204
Giannios, D. 2013, MNRAS, 431, 355
Goyal, A. 2018, Galax, 6, 34
Guo, F., Li, H., Daughton, W., & Liu, Y.-H. 2014, PhRvL, 113, 155005
Hayashida, M., Nalewajko, K., Madejski, G. M., et al. 2015, ApJ, 807, 79
H. E. S. S. Collaboration, Abramowski, A., Acero, F., et al. 2010, A&A, 520, A83
Joshi, M., & Böttcher, M. 2011, ApJ, 727, 21
Kalberla, P. M. W., Burton, W. B., Hartmann, D., et al. 2005, yCat, 8076, 0
Khatoon, R., Shah, Z., Misra, R., & Gogoi, R. 2020, MNRAS, 491, 1934
Kirk, J. G., & Mastichiadis, A. 1999, APh, 11, 45
Kun, E., Jaroschewski, I., Ghorbanietemad, A., et al. 2022, ApJ, 940, 163
Kushwaha, P., Chandra, S., Misra, R., et al. 2016, ApJL, 822, L13
Kushwaha, P., & Pal, M. 2020, Galax, 8, 66
Kushwaha, P., Sahayanathan, S., Lekshmi, R., et al. 2014, MNRAS, 442, 131
Liao, N. H., Bai, J. M., Liu, H. T., et al. 2014, ApJ, 783, 83
Liodakis, I., Romani, R. W., Filippenko, A. V., et al. 2018, MNRAS, 480, 5517
Liodakis, I., Romani, R. W., Filippenko, A. V., Kocevski, D., & Zheng, W. 2019, ApJ, 880, 32
Liu, H. T., Bai, J. M., & Ma, L. 2008, ApJ, 688, 148
MacDonald, N. R., Marscher, A. P., Jorstad, S. G., & Joshi, M. 2015, ApJ, 804, 111
MAGIC Collaboration, Ahnen, M. L., Ansoldi, S., et al. 2018, A&A, 619, A45
Majumdar, J., Maurya, S., & Prince, R. 2025, arXiv:2504.18927
Mannheim, K., & Biermann, P. L. 1992, A&A, 253, L21
Maraschi, L., Ghisellini, G., & Celotti, A. 1992, ApJL, 397, L5
Mattox, J. R., Bertsch, D. L., Chiang, J., et al. 1996, ApJ, 461, 396
Max-Moerbeck, W., Hovatta, T., Richards, J. L., et al. 2014a, MNRAS, 445, 428
Max-Moerbeck, W., Richards, J. L., Hovatta, T., et al. 2014b, MNRAS, 445, 437
Meyer, M., Scargle, J. D., & Blandford, R. D. 2019, ApJ, 877, 39
Morris, P. J., Potter, W. J., & Cotter, G. 2019, MNRAS, 486, 1548
Mücke, A., & Protheroe, R. J. 2001, APh, 15, 121
Nolan, P. L., Abdo, A. A., Ackermann, M., et al. 2012, ApJS, 199, 31
Ojha, R., & Carpen, B. 2017, ATel, 9928, 1
Ojha, R., Carpenter, B., & Dutka, M. 2013, ATel, 4941, 1
Padovani, P. 2017, NatAs, 1, 0194

Paliya, V. S. 2015, ApJ, 804, 74
Polatidis, A. G., Wilkinson, P. N., Xu, W., et al. 1995, ApJS, 98, 1
Poutanen, J., & Stern, B. 2010, ApJL, 717, L118
Prince, R., Khatoon, R., & Stalin, C. S. 2021, MNRAS, 502, 5245
Prince, R., Majumdar, P., & Gupta, N. 2017, ApJ, 844, 62
Pursimo, T., Blay, P., Telting, J., & Ojha, R. 2017, ATel, 9956, 1
Rajput, B., Stalin, C. S., & Sahayanathan, S. 2020, MNRAS, 498, 5128
Rajput, B., Stalin, C. S., Sahayanathan, S., Rakshit, S., & Mandal, A. K. 2019, MNRAS, 486, 1781
Ramakrishnan, V., Hovatta, T., Nieppola, E., et al. 2015, MNRAS, 452, 1280
Ramakrishnan, V., Hovatta, T., Tornikoski, M., et al. 2016, MNRAS, 456, 171
Rani, B., Krichbaum, T. P., Fuhrmann, L., et al. 2013a, A&A, 552, A11
Rani, B., Lott, B., Krichbaum, T. P., Fuhrmann, L., & Zensus, J. A. 2013b, A&A, 557, A71
Razali, N. M., Wah, Y. B., et al. 2011, Journal of Statistical Modeling and Analytics, 2, 21
Ren, H. X., Cerruti, M., & Sahakyan, N. 2023, A&A, 672, A86
Robinson, J., & Böttcher, M. 2024, ApJ, 977, 42
Roming, P. W. A., Kennedy, T. E., Mason, K. O., et al. 2005, SSRv, 120, 95
Roy, N., Chatterjee, R., Joshi, M., & Ghosh, A. 2019, MNRAS, 482, 743
Sahakyan, N. 2018, ApJ, 866, 109
Sahayanathan, S., Sinha, A., & Misra, R. 2018, RAA, 18, 035
Scargle, J. D., Norris, J. P., Jackson, B., & Chiang, J. 2013, ApJ, 764, 167
Schlafly, E. F., & Finkbeiner, D. P. 2011, ApJ, 737, 103
Shah, Z., Jithesh, V., Sahayanathan, S., Misra, R., & Iqbal, N. 2019, MNRAS, 484, 3168
Shah, Z., Mankuzhiyil, N., Sinha, A., et al. 2018, RAA, 18, 141
Shah, Z., Sahayanathan, S., Mankuzhiyil, N., et al. 2017, MNRAS, 470, 3283
Shapiro, S. S., & Wilk, M. B. 1965, Biometrika, 52, 591
Sikora, M., Begelman, M. C., & Rees, M. J. 1994, ApJ, 421, 153
Sikora, M., Błażejowski, M., Begelman, M. C., & Moderski, R. 2001, ApJ, 554, 1
Sinha, A., Khatoon, R., Misra, R., et al. 2018, MNRAS, 480, L116
Tavecchio, F., Pacciani, L., Donnarumma, I., et al. 2013, MNRAS, 435, L24
Thekkoth, A., Baheeja, C., Sahayanathan, S., & , C. D. R. 2024, JHEAp, 42, 115
Timmer, J., & König, M. 1995, A&A, 300, 707
Tolamatti, A., Ghosal, B., Singh, K. K., et al. 2022, APh, 139, 102687
Trushkin, S. A., Mingaliev, M. G., Sotnikova, Y. V., et al. 2014a, ATel, 5792, 1
Trushkin, S. A., Mingaliev, M. G., Sotnikova, Y. V., et al. 2014b, ATel, 5869, 1
Urry, C. M., & Padovani, P. 1995, PASP, 107, 803
Vaughan, S., Edelson, R., Warwick, R. S., & Uttley, P. 2003, MNRAS, 345, 1271
Wang, G., Fan, J., Xiao, H., & Cai, J. 2022, PASP, 134, 104101
Wang, G. G., Cai, J. T., & Fan, J. H. 2022, ApJ, 929, 130
Zhang, Y. H., Treves, A., Celotti, A., Qin, Y. P., & Bai, J. M. 2005, ApJ, 629, 686
Zhou, R. X., Zheng, Y. G., Zhu, K. R., Kang, S. J., & Li, X. P. 2024, ApJ, 962, 22